Multi-tissue mesh generation for brain images*

Yixun Liu[1,2], Panagiotis Foteinos[1,2], Andrey Chernikov[2], and Nikos Chrisochoides[2]

[1]Department of Computer Science, The College of William and Mary,
{enjoywm, pfot}@cs.wm.edu
[2]Department of Computer Science, Old Dominion University,
{andrey.n.chernikov, npchris}@gmail.com

Summary. We develop a multi-tissue mesh generation method that is suitable for finite element simulation involved in non-rigid registration and surgery simulation of brain images. We focus on the following four critical mesh properties: tissue-dependent resolution, fidelity to tissue boundaries, smoothness of mesh surfaces, and element quality. Each mesh property can be controlled on a tissue level. This method consists of two steps. First, a coarse multi-tissue mesh with tissue-dependent resolution is generated according to a predefined subdivision criterion. Then, a tissue-aware point-based registration method is used to find an optimal trade-off among fidelity, smoothness, and quality. We evaluated our method on a number of images ranging from MRI, visible human, to brain atlas. The experimental results verify the features of this method.

1 Introduction

Multi-tissue mesh generation of medical images is a necessary procedure for building a heterogeneous biomechanical model, which has numerous applications such as physical model-based non-rigid registration, segmentation and surgery simulation. However, there is little literature addressing this issue so far.

Several groups [1, 2, 3] presented multi-tissue mesh generation methods based on Delaunay refinement. However, elements with small dihedral angles (a.k.a, slivers) are likely to occur in Delaunay meshes, because elements are removed only when their radius-edge ratio is large; their dihedral angle quality is completely ignored. Meyer et al. [3] showed at least 0.6% slivers occurred in their experiments on frog data. Boltcheva et al. [1] and Pons et al. [2] employed sliver exudation postprocessing technique [4] to remove slivers and showed very good quality mesh (minimal dihedral angle is larger than 4 degrees).

*This work is supported in part by NSF grants: CCF-0916526, CCF-0833081, and CSI-719929 and by the John Simon Guggenheim Foundation.

Unlike these Delaunay-based methods, Zhang et al. [5] presented an octree-based method to generate a tetrahedral and hexahedral mesh. This method first identifies the interface between two or several different tissues and non-manifold nodes on the boundary. Then, all tissue regions are meshed with conforming boundaries simultaneously. At last, edge-contraction and geometric flow schemes are used to improve the quality of the tetrahedral mesh. In our work, we incorporate mesh quality, smoothing and fidelity into one point based registration (PBR) framework.

Molino et al. [6] presented a crystalline, red green strategy for mesh generation. This method starts with a Body-Centered Cubic (BCC) mesh and then deforms it to match the object boundary. The geometry is represented by signed distance function and the refinement is performed by a red green strategy. This BCC-based approach shows a very good quality of the mesh, because the quality of BCC mesh is high and its regular refinement still leads to a BCC mesh. However, this approach is limited to a single tissue.

The contribution of this paper is a novel mesh generation method which is characterized by *1) multi-tissue mesh, 2) tissue-dependent resolution, 3) natural control of the trade-off among quality, fidelity, and smoothness on tissue level.*

2 Method

Our approach requires multi-label images as input, in which label 0 denotes the background, and positive integers indicate different tissues. The approach consists of two steps: coarse mesh generation (CMG) and tissue-aware PBR as shown in Fig. 1. CMG includes two substeps,

1. BCC mesh.
   Use BCC mesh to subdivide the object space into connected tetrahedra. Note that this step does not distinguish different tissues. All tissues with label larger than zero belong to the same object (non-background object). The resulting BCC mesh is homogeneous.
2. Coarse tissue dependent resolution multi-tissue mesh generation (CMesh).
   This step specifies which tissue each tetrahedron belongs to and then yields a submesh for each tissue. Each tissue is capable of automatically adjusting its resolution based on its geometrical complexity and the predefined subdivision criterion.

The resulting coarse multi-tissue mesh of step I includes different submeshes and each submesh has its own resolution. The discrepancy between the surface of the submesh and its corresponding boundary in the multi-label image is corrected by a tissue-aware PBR method. This step includes three substeps.

1. detect edges for each tissue in the multi-label image to obtain target point set.

2. extract surface nodes for each submesh to obtain source point set.
3. deform the surface of each submesh to its corresponding boundary based on PBR.

The framework of this approach is shown in Fig. 1. Each step listed in this framework will be discussed in detail in the following sections.

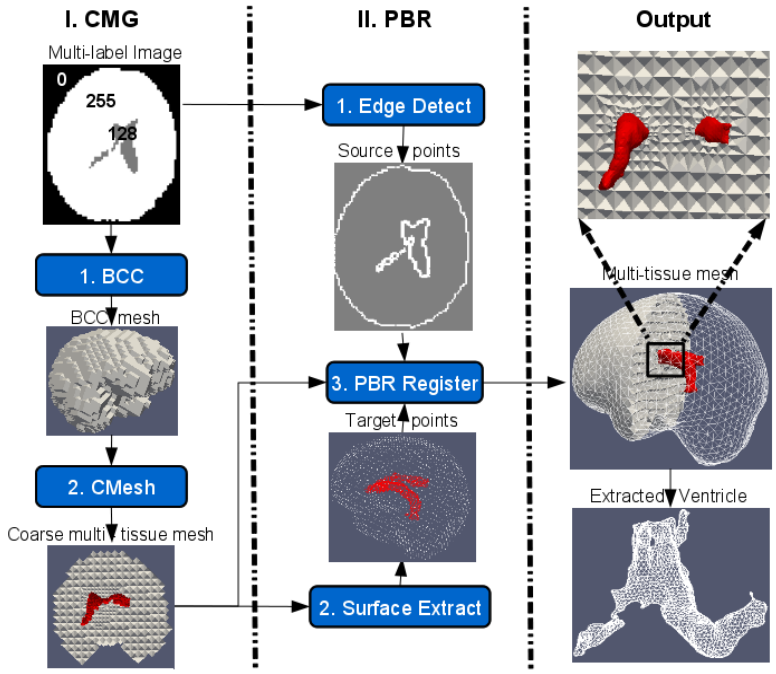

Fig. 1. Multi-tissue mesher framework.

2.1 Coarse mesh generation

The purpose of the coarse mesh generation is to obtain the source points, which will be used in the tissue-aware PBR method. The coarse mesh needs to take into account the following criteria: 1) multi-tissue input, 2) good conditioning for the subsequent PBR, and 3) fewer tetrahedra.

This part includes two steps as shown in Fig 1. Body-Centered Cubic provides an initial lattice, which has been well documented in [7, 6]. For the completeness of this paper, we will briefly describe its properties and red green subdivision, and then focus on how CMesh generates and refines submeshes.

BCC mesh

BCC mesh is an actual crystal structure ubiquitous in nature. It is highly structured and easily refined initially or during the simulation. The nodes of BCC are grid points of two interlaced grids like the blue grid and the green grid in Fig. 2(a). The edges of BCC consist of edges of the grid and additional edges between a node and its eight nearest neighbors in the other grid.

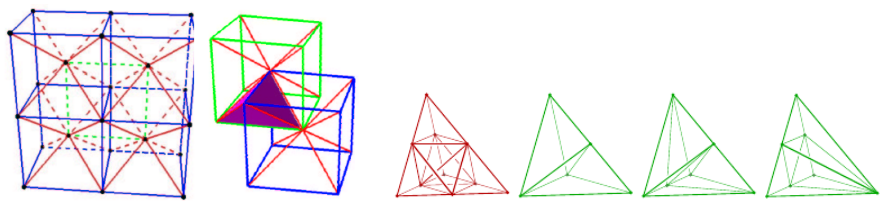

(a) A portion of the BCC lattice. (b) Red-greed subdivision

Fig. 2. BCC lattice and red green subdivision (These two figures come from [6]).

The refinement of BCC mesh is performed by a red green strategy. Initially, all BCC lattice tetrahedra are labeled with red. A red tetrahedron can be subdivided into eight children (1:8 refinement) and each child is labeled with red as shown in Fig. 2(b). There are three choices for the internal edge of the tetrahedron. If the shortest one is selected, the resulting eight child tetrahedra are exactly the BCC tetrahedra except the size is one half of the original BCC. So, the quality of the refined mesh can be guaranteed using this red (regular) subdivision. This is the reason that we select BCC as the initial tetrahedral mesh, although our method is general enough to start from any tetrahedral mesh. This red subdivision will lead to T-junctions at the newly-created edge midpoints where neighboring tetrahedra are not refined to the same level. To remove the T-junctions, green subdivision, including three cases, is performed. These three cases are,

1. there is one edge with T-junction
2. there are two opposite edges with T-junctions
3. there are three edges of a face with T-junctions

The green subdivision according to these three cases is shown in Fig. 2(b). All the child tetrahedra of the green subdivision are labeled with green. This irregular green subdivision will reduce the quality of the tetrahedron, so all the child tetrahedra will be removed and red subdivision is performed on their red parent when higher resolution is desired.

CMesh

CMesh is used to identify the submesh for each tissue in BCC mesh and subdivide it if necessary. We define a label operation table, based on which label

redistribution method is used to produce different submeshes. A predefined subdivision criterion is used to determine which submesh needs to be further subdivided. If a submesh needs to be subdivided, in order to reduce the number of the tetrahedra, only its boundary tetrahedra are further subdivided (multi-resolution).

In Fig. 3, we illustrate how CMesh identifies and subdivides submeshes. First, CMesh assigns each tetrahedron with a label of the tissue, to which most part of the tetrahedron belongs (Fig. 3(a)). As a result, an initial multi-tissue mesh is produced. However, this multi-tissue mesh is not well conditioned for subsequent deformation, because more than one face, i.e., four nodes of one tetrahedron are probably on the interface. We term this kind of tetrahedron as a bad conditioned tetrahedron. In this case, deforming four nodes easily crushes this tetrahedron. We prefer a submesh only with two kinds of tetrahedra: inner tetrahedron (no faces on the interface) and boundary tetrahedron (only one face on the interface). To reach this end, we redistribute the label of the bad conditioned tetrahedra according to the operations defined in Table 1 to generate a well conditioned multi-tissue mesh (Fig. 3(b)). After label redistribution, we check if each submesh needs to be further subdivided. If it satisfies the criterion for the resolution, defined in Fig. 3(e), the algorithm stops, otherwise subdivides (Fig. 3(c)) and redistributes labels (Fig. 3(d)). Repeat the above procedures until the desired resolution is reached. The submesh produced by this label redistribution method not only has good conditioning, but also reaches conformity with its neighboring submeshes.

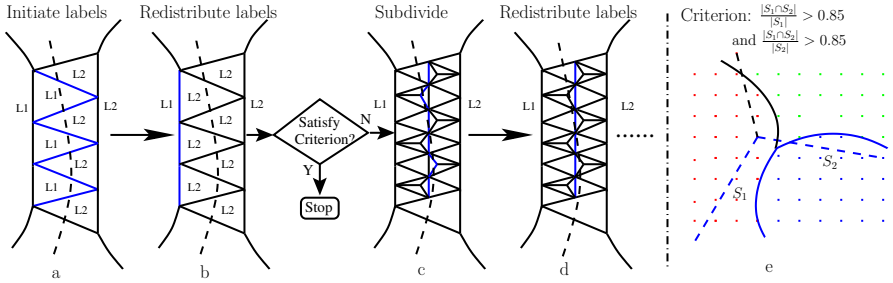

Fig. 3. Coarse multi-tissue mesh generation. (a) L1 and L2 are tissue labels, the dash line is the real boundary and the blue line is the submesh interface. (b) Redistribute labels according to operation table 1. (c) Subdivide if not satisfy the resolution criterion defined in (e). (d) Redistribute labels again. (e) Resolution criterion: 0.85 is the subdivision threshold, an experiment value evaluated on MRI ,visible human and brain atlas. Points represent voxels and colors represent different tissues. S_1 is the voxel set within the blue submesh (blue dash lines) and S_2 is the voxel set within the blue tissue (blue curves).

Operation table The operation table decides how to redistribute the label of a tetrahedron based on its relation, termed as configuration, with face-adjacent tetrahedra. The purpose of the operations defined in Table 1 is to move the bad conditioned tetrahedra to its neighboring submeshes. If all the bad conditioned tetrahedra are removed from one submesh, this submesh and its neighboring submeshes will reach good conditioning at the same time. We clarify this point by taking case 5 defined in table 1 as an example. If the four face-adjacent tetrahedra of a given tetrahedron T have labels: $< L, L1, L1, L1 >$, denoted as $< L, 3L1 >$ for simplicity, the label of T will be reassigned with $L1$ because its three faces are on the interface between submesh L and $L1$. Fig. 3 uses case 5 for redistribution. Because we use 2D triangles instead of 3D tetrahedra in Fig. 3, case 5 is degenerated from $< L, 3L1 >$ to $< L, 2L1 >$. In summary, the operations defined in Table 3 move a tetrahedron to its face-adjacent submesh if this tetrahedron is not an inner (case 1) or boundary tetrahedron (case 2). As a result, no tetrahedra with more than one face on the boundary exist, which leads to a well conditioned mesh for the subsequent deformation.

Table 1. Operation case table for tetrahedron T with label L.

Case	1	2	3	4	5	6	7
Configuration	4L	3L,1L1	2L,2L1	2L,1L1,1L2	1L,3L1	1L,L1,2L2	1L,1L1,1L2,1L3
Operation	T=inner tetra	T=boundary tetra	T.label=L1	T.label=L1	T.label=L1	T.label=L2	T.label=L1

Criteria for subdivision In multi-label image, a tissue is defined with a set of voxels with the same intensity, say L. Heuristically, the closer the surface of a submesh is to the boundary of a tissue, the more voxels of the tissue are located in the submesh and the more voxels with label L this submesh has. To quantitatively evaluate the similarity between the sbumesh and the tissue region, we define two voxel sets,

1. $S1$: all the voxels in the submesh (the points within two dash lines in Fig. 3 (e)).
2. $S2$: all the voxels in the tissue region (the points within the curve in Fig. 3 (e)).

$S_1 \cap S_2$ define the point set shared by the submesh and the tissue region. We expect the common region to be similar with the submesh and the tissue region. We use $\frac{|S_1 \cap S_2|}{|S_1|}$ to measure the similarity between the common region and the submesh, and $\frac{|S_1 \cap S_2|}{|S_2|}$ to measure the similarity between the common region and the tissue region. So, the subdivision criterion can be defined as,

$$\frac{|S_1 \cap S_2|}{|S_1|} < threshold \quad and \quad \frac{|S_1 \cap S_2|}{|S_2|} < threshold \tag{1}$$

where *threshold* is an input parameter. $0 \leq \frac{|S_1 \cap S_2|}{|S_1|} \leq 1.0$ and $0 \leq \frac{|S_1 \cap S_2|}{|S_2|} \leq 1.0$, so $0 \leq threshold \leq 1.0$.

The reason that we simultaneously use two values as the criterion is to avoid case a and case b in Fig. 4. Moreover, that we do not simply use $\frac{|S_1|}{|S_2|}$ is in order to avoid case c in Fig 4.

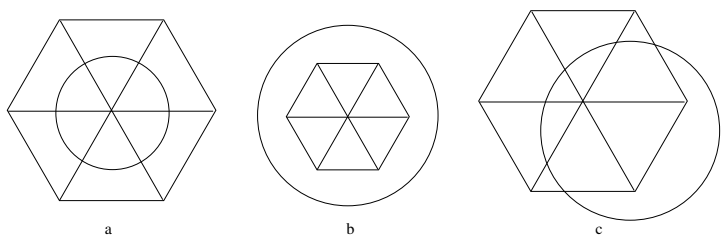

Fig. 4. Three special cases. The circle represents the tissue region and the polygon represents the submesh. For simplicity, the voxels are not shown. All these three cases show a big discrepancy between the tissue boundary and the submesh boundary. However, for case (a), because the tissue is totally covered by the submesh, $\frac{|S_1 \cap S_2|}{|S_2|}$ has the highest value 1.0. For case (b), because the submesh is totally covered by the tissue region, $\frac{|S_1 \cap S_2|}{|S_1|}$ has the highest value 1.0. For case (c), $\frac{|S_1|}{|S_2|}$ can be equal to be 1.0, if the submesh and tissue region have the same number of voxels.

The criterion relies on the number of the voxels, and therefore it is susceptible to the resolution of the multi-label image. For instance, if the resolution is very low, we cannot find any voxels in a tetrahedron. To overcome this difficulty, the up-sampling is performed automatically if no voxels are detected in a tetrahedron. To improve the performance, we do not perform up-sampling in the whole image, but restrict it to the bounding box of the tetrahedron.

2.2 Tissue-aware PBR

This step is used to 1) deform the coarse mesh close to the boundary, 2) maintain the quality of the coarse mesh, and 3) generate a smooth mesh. The coarse mesh needs to be deformed to the boundary. Unlike the interpolation method used in [6], we treat the deformation as a point based registration. This method iteratively deforms the mesh towards the boundary of the multi-label image. In each iteration, the deformation will be viewed as a point based registration problem. Each surface of the submesh will be registered with its corresponding boundary in the image. The advantage of this approach is the quality, smoothing and fidelity can be incorporated into the same registration framework.

Source point set and target point set

Two point sets are needed in this registration framework: source and target point sets. The source points are the surface nodes of the mesh and the target points are the edge points in the multi-label image. The source point set is obtained by extracting the surface nodes of each submesh. The target point set is obtained by canny edge detection, which is facilitated by ITK implementation [8]. For each source point, the target point closest to it will be viewed as its potential correspondence. It is computationally intensive to search the closest point in all the target points. We associate each source/target point with a label to denote which tissue it belongs to, and therefore the search is only restricted to the target points, which have the same label with the source point.

Figure 5 shows the source point set and the target point set produced by visible human data. These intermediate results for other data will not be shown in Section results.

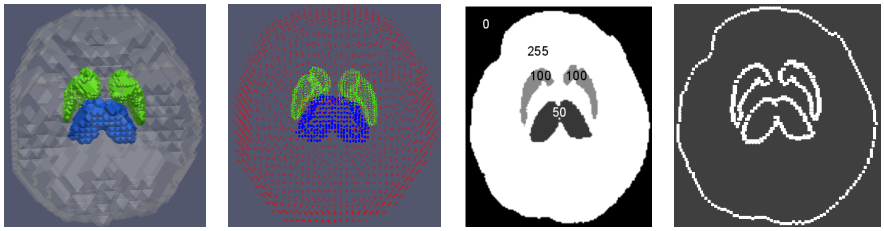

(a) Coarse multi-tissue mesh (b) Source point set (c) Multi-label image (d) Target point set

Fig. 5. Point sets. The source point set (b) include all the surface nodes of the coarse mesh (a) and the target point set (d) are the edge points in the multi-label image (c).

Register source points with target points

The classic PBR [9] is used to register two images, floating image and reference image. The PBR is based on the concept of energy minimization. A sparse set of registration points within the floating image are identified. The displacement between the floating and the reference images is estimated using Block Matching [10] at each registration point. These displacements are applied as boundary condition on a biomechanical model to derive the entire brain deformation.

In our work, we extend this PBR method and use it in the mesh generation field. In our mesh generation, the registration points will be fixed to the nodes

of the mesh instead of the feature points. The displacement of these registration points is estimated by taking fidelity, smoothing and quality into account. The homogeneous biomechanical model used in [9] is generalized with a more flexible tissue-aware model as shown below,

$$W(U) = \sum_{i=1}^{n} (U^T K_i U + \lambda_i (H_i U - D_i)^T (H_i U - D_i)), \tag{2}$$

where n is the number of the tissues; K_i is the global stiffness matrix assembled by the tetrahedra within i-th tissue. K_i is related with two biomechanical attributes of i-th tissue: Young's modulus and Possion's ratio. The building of K_i has been well documented in [11]. H_i is the global linear interpolation matrix assembled by registration points.

Each registration point o_k with number k contained in tetrahedron with vertex numbers $c_i, i \in [0:3]$ has contribution to four 3×3 submatrices: $[H]_{kc_0}, [H]_{kc_1}, [H]_{kc_2}, [H]_{kc_3}$. $[H]_{kc_i}$ is defined as: $[H]_{kc_i} = diag(h_i, h_i, h_i)$. The linear interpolation factor h_i is calculated as:

$$\begin{bmatrix} h_0 \\ h_1 \\ h_2 \\ h_3 \end{bmatrix} = \begin{bmatrix} v^x_{c_0} & v^x_{c_1} & v^x_{c_2} & v^x_{c_3} \\ v^y_{c_0} & v^y_{c_1} & v^y_{c_2} & v^y_{c_3} \\ v^z_{c_0} & v^z_{c_1} & v^z_{c_2} & v^z_{c_3} \\ 1 & 1 & 1 & 1 \end{bmatrix}^{-1} \begin{bmatrix} o^x_k \\ o^y_k \\ o^z_k \\ 1 \end{bmatrix} \tag{3}$$

where v_{c_i} is the node with number c_i. Because we use the node as the registration point, which means o_k is same with one of the four nodes, equation 4 is reduced to,

$$h_i = \begin{cases} 1 & \text{for } o_k = v_{c_i} \\ 0 & \text{for } o_k \neq v_{c_i} \end{cases} \tag{4}$$

U is the global unknown displacement vector at the mesh nodes; D_i is the distance vector at the i-th surface nodes. The first term of the energy function represents the biomechanical strain energy, a measure of the mesh deformation. The second term represents the matching error between source point set and target point set, a measure of the fidelity.

We term energy function (2) as a tissue-aware model, because it is able to use λ_i to balance the quality and fidelity for i-th tissue no matter this model is homogeneous (same Young's modulus and Possion's ratio for all tissues) or not.

Distance vector D, for simplicity omitting subscript i, reflects the fidelity between source points and target points. To incorporate smoothing into the registration framework, we calculate D according to the relaxed target position by classic Laplacian smoothing. Generally, mesh smoothing is performed as a postprocessing after the mesh generation. However, this will lead to the smoothing out of control of the biomechanical model, so we reflect the smoothing as we calculate D and therefore naturally incorporate it into the energy function (2). The i-th entry d_i of distance vector D is calculated as follows.

Let the source point corresponding to d_i be s, its normal be n and the set of its neighboring nodes be S. The normal n is calculated by averaging the normals of the surface faces, which share the source point s. For each point $p_i \in S$, calculate its closest target point $t_i, i = 1 \ldots m$. For s, calculate its closest target point q. The relaxed (smoothed) position of s is $s' = \frac{\sum_{k=1}^{k=m} t_i + q}{|S|+1}$. Projecting $s' - s$ onto the normal of s leads to

$$d_i = (\frac{\sum_{k=1}^{k=m} t_k + q}{\mid S \mid +1} - s) \cdot n \tag{5}$$

We illustrate the calculation of d_i in Fig. 6.

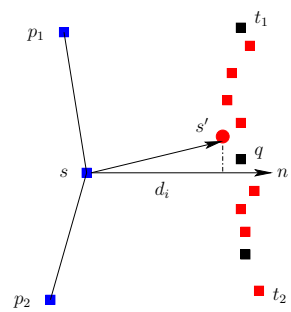

Fig. 6. The calculation of d_i of node s. p_1 and p_2 are two neighboring nodes of s. t_1, t_2 and q are the closets points corresponding to p_1, p_2, s respectively. Their average position is s'. Project $s' - s$ on unit normal n of node s to produce d_i.

We minimize $W(U)$ by solving

$$\frac{\partial W}{\partial U} = 0 \Rightarrow \sum_{i=1}^{i=n} (K_i + \lambda_i H_i^T H_i) U = \sum_{i=1}^{i=n} \lambda_i H_i^T D_i \tag{6}$$

Once we obtain U, we can update the positions of the nodes of the mesh. This procedure will be repeated until the average error between source points and target points is below a predefined tolerance or the iteration reaches maximum number. The average error is evaluated by,

$$\bar{d} = \frac{\sum \|s_i - t_i\|}{\mid S \mid}, \tag{7}$$

where s_i is a source point; t_i is the closest target point of s_i, and S is source point set. This average error is also used to evaluate the fidelity in Section 3.

The whole method including coarse mesh generation and PBR based deformation is presented in Algorithm 1.

Algorithm 1 MULTI-TISSUE MESH GENERATION

M=MultiTissueMesher($MultiLabelImage, tolerance$)

Require: $MultiLabelImage, tolerance$
Ensure: M: tissue dependent resolution multi-tissue mesh

```
Coarse Mesh Generation:
Generate BCC mesh M
Assign label for each tetrahedron in M
repeat
    Label redistribution according to Table 1 to yield multi-tissue mesh M
    for each subMesh do
        if satisfy the subdivision criterion (equation (1)) then
            Subdivide M along the boundary using red green strategy
        end if
    end for
until no subdivision
PBR Deformation:
Generate source point set by surface extraction from M
Generate target point set by edge detection from MultiLabelImage
repeat
    Calculate D_i using equation (5)
    Assemble K_i
    Assemble H_i using equation (4)
    Solve U using equation (6)
    Deform M using M ⇐ M + U
    Calculate error d̄ using equation (7)
until reach maximum iteration or d̄ < tolerance
Remove the tetrahedra with label 0 from M
```

3 Results

To fully evaluate this method, we first conduct experiment on MRI, which includes two tissues: brain and ventricle. Then, we use two nerves in visible human data to evaluate the tissue-aware quality control. At last, we qualitatively and quantitatively evaluate this method on a non-manifold data, brain atlas.

3.1 Real MRI

The ventricle has different biomechanical attributes from other tissues in the brain, and so it is often used to build a heterogeneous biomechanical model [12]. We evaluate our method on this simple heterogeneous model: the ventricle and the rest of the brain, in which the Young's modulus $E = 10Pa$, Poisson's ratio $\nu = 0.1$ for ventricle, and $E = 3000Pa$, $\nu = 0.45$ for the rest of the brain [12]. The results are shown in Fig. 7. Fig. 7(a) is the multi-label image, in which label 128 and 255 denote the ventricle and the brain respectively. Fig. 7(b) is the coarse multi-tissue mesh and Fig. 7(c) is the

final (deformed) multi-tissue mesh. The deformed mesh is cut through and zoomed in as Fig. 8(a). Fig. 8(b) is the wireframe view of two submeshes and Fig. 8(c) is the extracted ventricle. The subdivision threshold we used to produce Fig. 7(b) is 0.85. With this parameter, the outer boundary of the brain is not further subdivided, but its inner interface with the ventricle is subdivided twice. Fig. 8(b) clearly shows that the ventricle has higher resolution than the brain.

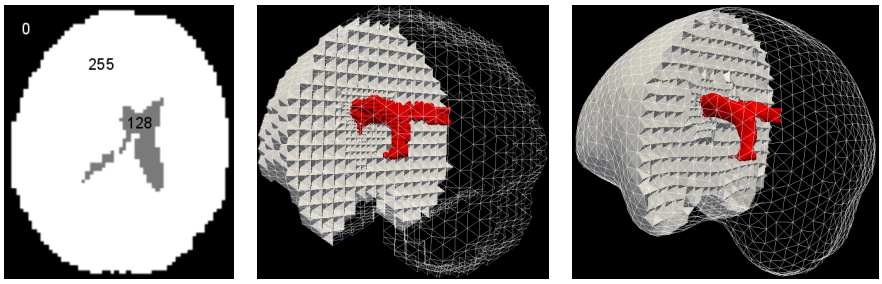

(a) Multi-label image (b) Coarse mesh (c) Final mesh

Fig. 7. Multi-tissue mesh generation for MRI data. (a) is the multi-label image. The coarse multi-tissue mesh (b) is generated with subdivision threshold 0.85. (c) is the deformed multi-tissue mesh. The numbers of source points and target points are 4497 and 31241 respectively.

From Fig. 7(a), we can see that the segmented brain and ventricle are not smooth, but the brain submesh (Figure 7(c)) and the extracted ventricle submesh (Figure 8(c)) are very smooth. It demonstrates that this method has a low requirement for the segmentation due to the incorporation of the smoothing into the PBR framework.

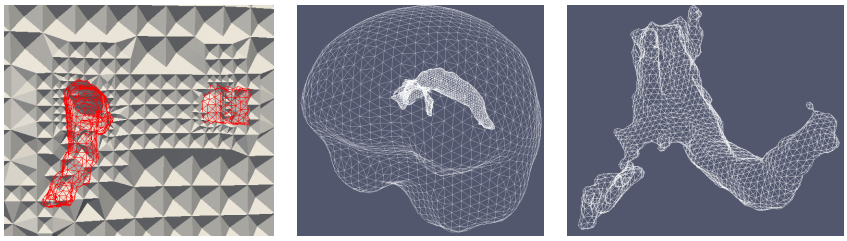

(a) Closeup (b) Wireframe view (c) Extracted ventricle

Fig. 8. (a) is the closeup of the inner. (b) is the wireframe view of the two submeshes and (c) is the extracted ventricle.

To show the conformity of the interfaces, we first extract two submeshes: the brain and the ventricle. The extracted brain is shown in Fig. 9(a), in which the hole is induced by the extracted ventricle. The extracted ventricle is shown in Fig. 9(b). We want to insert the ventricle into the hole to show the conformity on the interface between the ventricle surface and the hole surface, so the ventricle surface should not be too smooth to distinguish surface triangles, otherwise the conformity is not easily to be observed.

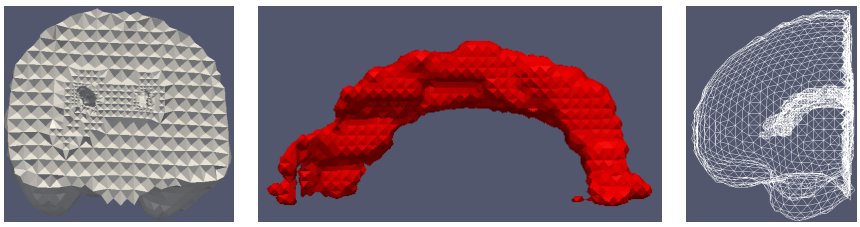

(a) Ventricle hole (b) Ventricle Surface (c) Hole wireframe

Fig. 9. (a) is the brain with a ventricle hole. (b) is the extracted ventricle surface. (c) is the wireframe view of the hole. The front surfaces of the brain are culled to show the hole.

To show the conformity, we need to visualize the two surfaces on the interface simultaneously. So, the hole should be visualized in a different way from the ventricle. We use wireframe to show the hole as Fig. 9(c). Note that the front surface of the brain in Fig. 9(c) is culled to clearly show the hole. Fig. 10(a) is the result by inserting the ventricle into the hole. Fig. 10(b) is the closeup of the interface of the two surfaces. We conducted our experiment on Dell PowerEdge (2 x dual-core Opteron 2218, 2.6 GHz CPU) and the runtime is about 5 minutes.

3.2 Visible human

We also evaluate our method using visible human data[2]. Its multi-label image is shown in Fig. 11(a). This data includes three tissues: two nerves (dorsal thalamus (DT) with label 50 and caudata nucleus (CN) with label 100) and the brain with label 255. Fig. 11 and Fig. 12 show the results of this data. We use the same subdivision threshold 0.85 for this data. Fig. 12(b) and Fig. 12(c) clearly demonstrates the tissue-dependent resolution: nerve CN with resolution 1 (subdivided once), nerve DT with resolution 2 and the brain with resolution 0.

We use this data for the evaluation of the tissue-aware control of the quality. The results are shown in Fig. 13. The top three figures are the closeup

[2] http://www.nlm.nih.gov/

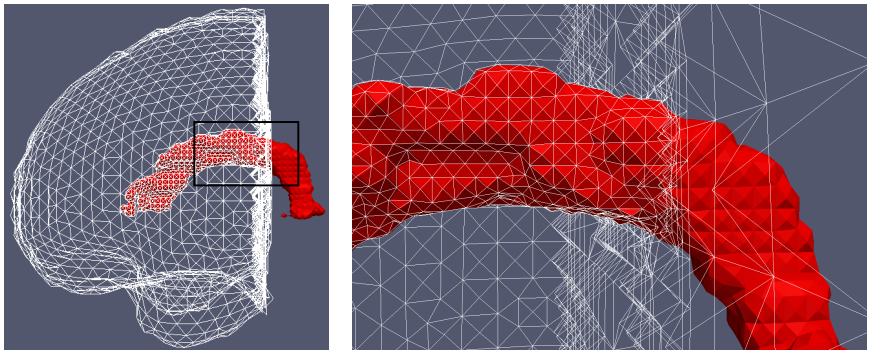

(a) Conformity (b) Closeup

Fig. 10. (a) shows the conformity of the interface. The part in the rectangle is enlarged in (b).

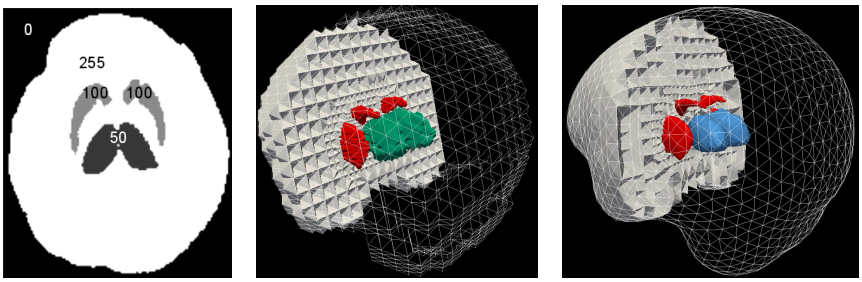

(a) Multi-label image (b) Coarse mesh (c) Final mesh

Fig. 11. Multi-tissue mesh generation for visible human data. (a) is the multi-label image. The coarse multi-tissue mesh (b) is generated with subdivision threshold 0.85. (c) is the deformed multi-tissue mesh. The numbers of source points and target points are 5828 and 26060 respectively.

of DT and CNP ($\lambda_{DT} = \lambda_{CNP} = 1.0$), the dihedral angle distribution of the tissue DT and the dihedral distribution of the tissue CNP. The bottom three figures are the results as we fix λ_{CNP}, but reduce λ_{DT} to 0.25. The left two figures do not show big difference, but the two middle figures clearly show the quality of DT improves from [13.6,76.1] to [15.1,80.6], because we pay more attention to the quality of DT. The two right figures do not show any big difference because we do not change λ_{CNP}. Compared to MRI experiment, more time is needed (9 minutes), because more tissues are involved.

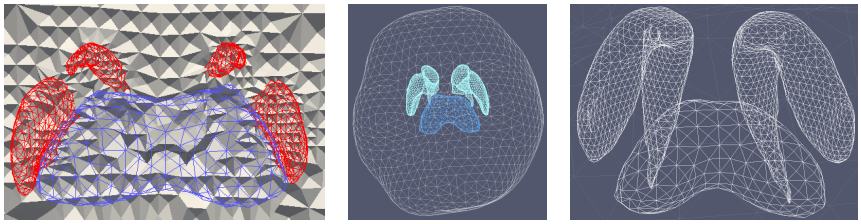

(a) Closeup (b) Wireframe view (c) Extracted two nerves

Fig. 12. (a) is the closeup of the inner. (b) is the wireframe view of the three submeshes and (c) is the extracted two nerves.

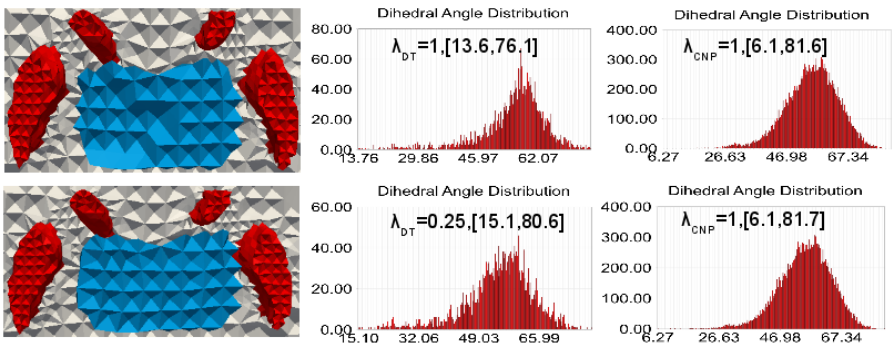

Fig. 13. Tissue-aware quality control. The two values in the bracket are minimum and maximum dihedral angles.

3.3 Brain atlas

We use brain atlas[3] to evaluate this method on non-manifold surfaces. The multi-label image is shown in Fig. 14(a) and the final multi-tissue mesh, produced with the same trade-off parameters ($\lambda_1 = \lambda_2 = ...\lambda_6 = 1.0$), is shown in Fig. 14(b).

We zoom in the interfaces of these tissues to show the conformity in Fig. 15 in a different point of view from Fig. 10. Fig. 16 has three subfigures and shows the fidelity, tissue-dependent resolution, and quality respectively. The fidelity part shows the comparison of the fidelity before PBR (left) and after PBR (right). The figure is generated by cutting through the mesh and overlapping it with the same slice of the multi-label images. The black arrows point to the places where bigger improvement of the fidelity occurs. Compared with the inner structures, the brain shows bigger improvement of the fidelity. The reason is, compared with the inner structures, the brain has lower resolution and therefore lower fidelity. Since we do not pay more attention to the inner structures (the same λ_i for all tissues), the tissue with lower fidelity improves

[3] http://www.spl.Harvard.edu/publications/item/view/1265

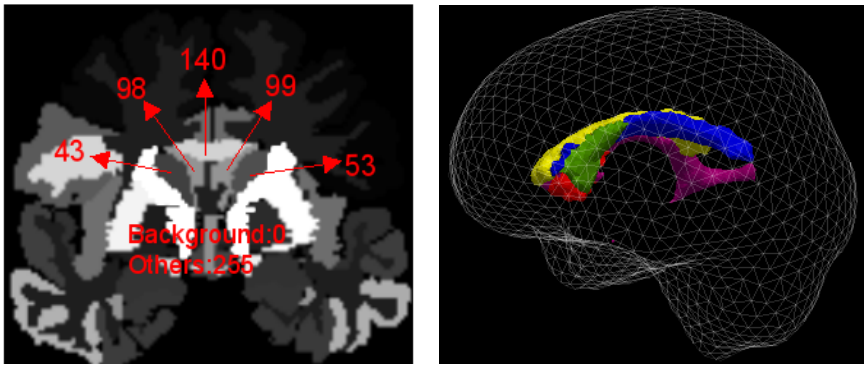

(a) Brain atlas (b) Final multi-tissue mesh

Fig. 14. Multi-tissue mesh for brain atlas. Five tissues along with the rest of the brain (a) are discretized. 43: right caudata nucleus (RCN), 53: left caudata nucleus (LCN), 98: right anterior horn of lateral ventricle (RAHLV), 99: left anterior horn of lateral ventricle (LAHLV), 140: corpus callosum (CC). The numbers of source points and target points are 6225 and 39136 respectively.

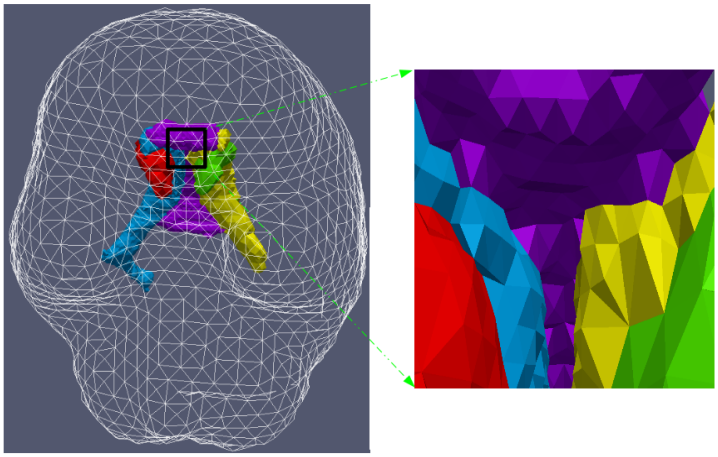

Fig. 15. Conformity of interfaces.

fidelity more. The fidelity is evaluated using equation (7) and listed in Table 2. In resolution part, the mesh is cut through to show the tissue-dependent resolution. In quality part, we present the distribution of the dihedral angle and aspect ratio under different trade-off parameter λ ($\lambda_1 = \lambda_2 = ...\lambda_6 = \lambda$). The values in brackets are the minimum and the maximum values for the whole mesh. The values for each submesh are listed in Table 2. As we increase λ from 1.0 to 1.5, i.e, paying less attention to the quality, the minimum dihedral angle reduces from 4.57 to 3.96 and the maximum aspect ratio increases from

8.80 to 15.83. It takes about 14 minutes to generate the final multi-tissue mesh.

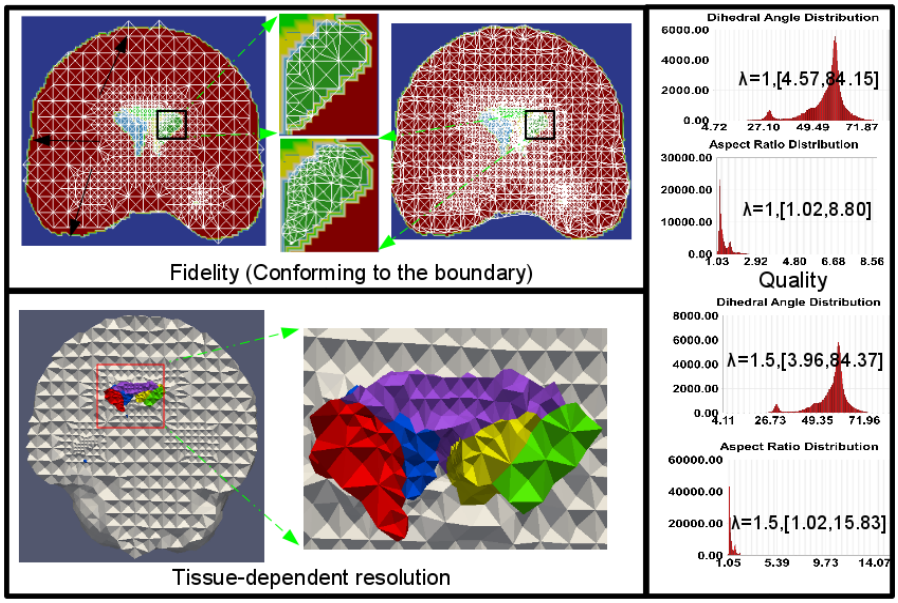

Fig. 16. The evaluation of fidelity, tissue dependent resolution and quality on the brain atlas.

A good quality mesh is characterized by the absence of slivers, i.e., tetrahedra with a very small dihedral angle, or aspect ratio close to 1. One observation from quality part is the number of the tetrahedra with ratio around 1 increases from 20000 to 40000 even when we pay less attention to the quality (increase λ from 1 to 1.5). This can be explained by the reason that lots of tetrahedra happen to improve their quality as deformed to the boundary.

Table 2. Quantitative evaluation for the multi-tissue mesh on the brain atlas. The atlas is regularized as spacing: $1mm \times 1mm \times 1mm$, size: $240 \times 240 \times 259$. The parameters are: subdivision threshold=0.85, $\lambda = 1.0$.

Nerve structures	RCN	LCN	RAHLV	LAHLV	CC	Other (brain)
Aspect ratio (Quality)	[**1.03**,3.75]	[**1.07**,3.01]	[**1.02**,6.84]	[**1.03**,4.07]	[**1.03**,3.96]	[**1.02**,8.80]
Dihedral angle (Quality)	[**13.36**,79.80]	[**24.7**,72.60]	[**10.06**,79.12]	[**17.74**,78.40]	[**13.56**,78.14]	[**4.57**,84.15]
Average distance (Fidelity)	0.80	0.91	0.79	0.82	0.82	0.99
Number of tetras	2944	612	9480	3849	14937	109466
Number of nodes	814	220	2589	1136	3766	21407

4 Conclusion

This paper presents a BCC-based multi-tissue mesh generation approach. This method inherits the advantages of BCC lattice mesh and extends it to a multi-tissue mesher by dealing with conformity using label redistribution based on a predefined operation table. This method can reach tissue-dependent resolution by using red-green subdivision under the guide of a subdivision criterion. The flexible control of the quality, fidelity and smoothing is obtained by incorporating these properties into a PBR framework. The experiments on the data ranging from MRI, visible human, to brain atlas demonstrate the effectiveness of this method.

References

1. Boltcheva, D., Yvinec, M., Boissonnat, J.D.: Mesh generation from 3d multi-material images. In: MICCAI. Volume 5762. (2009) 283–290
2. Pons, J.P., Ségonne, F., Boissonnat, J.D., Rineau, L., Yvinec, M., Keriven, R.: High-quality consistent meshing of multi-label datasets. In: Information Processing in Medical Imaging. Volume 4584. (2007) 198–210
3. Meyer, M., Whitaker, R., Kirby, R.M., Ledergerber, C., Pfister, H.: Particle-based sampling and meshing of surfaces in multimaterial volumes. IEEE Transactions on Visualization and Computer Graphics **14(6)** (2008) 1372–1379
4. Cheng, S.W., Dey, T.K., Edelsbrunner, H., Facello, M.A., Teng, S.H.: Silver exudation. J. ACM **47**(5) (2000) 883–904
5. Zhang, Y., Hughes, T.J., Bajaj, C.L.: An automatic 3d mesh generation method for domains with multiple materials. Computer Methods in Applied Mechanics and Engineering **199**(5-8) (2010) 405 – 415
6. Molino, N., Bridson, R., Teran, J., Fedkiw, R.: A crystalline, red green strategy for meshing highly deformable objects with tetrahedra. In: International Meshing Roundtable. (2003) 103114
7. Glazer, A.M., Burns, G.: Space Groups for Solid State Scientists. Academic Press, Inc., Philadelphia, PA, USA (1990) 2nd ed.
8. Kitware: http://www.itk.org/.
9. Clatz, O., Delingette, H., Talos, I.F., Golby, A., Kikinis, R., Jolesz, F., Ayache, N., Warfield, S.: Robust non-rigid registration to capture brain shift from intra-operative MRI. IEEE Trans. Med. Imag. **24**(11) (2005) 1417–1427
10. Bierling, M.: Displacement estimation by hierarchical block matching. Proc. SPIE Vis. Comm. and Image Proc. **1001** (1988) 942951
11. Bathe, K.: Finite Element Procedure. Prentice-Hall (1996)
12. Wittek, A., Miller, K., Kikinis, R., Warfield, S.K.: Patient-specic model of brain deformation: Application to medical image registration. Journal of biomechanics **40**(4) (2007) 919–929